



Universiteit  
Leiden  
The Netherlands

## **Towards an ab-axis giant proximity effect using ionic liquid gating**

Atesci, H.

### **Citation**

Atesci, H. (2018, September 12). *Towards an ab-axis giant proximity effect using ionic liquid gating*. *Casimir PhD Series*. Retrieved from <https://hdl.handle.net/1887/65452>

Version: Not Applicable (or Unknown)

License: [Licence agreement concerning inclusion of doctoral thesis in the Institutional Repository of the University of Leiden](#)

Downloaded from: <https://hdl.handle.net/1887/65452>

**Note:** To cite this publication please use the final published version (if applicable).

Cover Page



Universiteit Leiden



The handle <http://hdl.handle.net/1887/65452> holds various files of this Leiden University dissertation.

**Author:** Atesci, H.

**Title:** Towards an ab-axis giant proximity effect using ionic liquid gating

**Issue Date:** 2018-09-12

## Chapter 8

# Towards an ionic liquid induced *ab*-axis giant proximity effect in continuous $\text{La}_{2-x}\text{Sr}_x\text{CuO}_4$ junctions

*The giant proximity effect has been an unconventional and puzzling part of high temperature superconductivity. It can lead to proximitized coupling between two superconducting leads over distances much larger than allowed by the conventional proximity effect. In this chapter, we report techniques and preliminary results of ionic liquid-induced long-range proximity effect on a continuous  $\text{La}_{2-x}\text{Sr}_x\text{CuO}_4$  film. Our results show that the proximity effect in the *ab* axis can extend over two orders of magnitude larger than the coherence length of the cuprate.*

## 8.1 Introduction

Cuprate superconductors have brought many controversies. Notably, the proximity effect in specific cuprate Josephson junctions has initially been observed to behave differently [13–16] than in their conventional superconductor Josephson junction counterparts. With the advent of advanced growth techniques [5], this anomaly has been confirmed [6, 7] and consequently termed the giant proximity effect (GPE). It is suggested that its explanation can be coupled to another controversial topic, namely the pseudogap, seen by some as a precursor to superconductivity [251], while others view it as a competition of different phases with the superconducting phase [252].

The GPE seems to appear in  $SS'S$  junctions, with the  $S'$  barrier having a lower  $T_{c'}$  than the  $S$  leads by means of doping, as shown in  $\text{La}_{2-x}\text{Sr}_x\text{CuO}_4/\text{La}_2\text{CuO}_{4+\delta}/\text{La}_{2-x}\text{Sr}_x\text{CuO}_4$  *c*-axis [6]. In such a setup, a supercurrent could be measured at  $T_{c'} < T < T_c$  over a distance of up to two orders of magnitude larger than the normal coherence length of  $S'$ , being 0.25 nm. No such long-range proximity effect was observed for  $\delta = 0$ . Long-range effects have also been observed in the vicinity of Pb islands on a Pb/Si(111) [21]. With spectroscopic methods using Scanning Tunneling Microscopy, the Pb monolayer locally was found to have a proximity-induced superconducting order parameter above its own bulk critical temperature.

Our interest is twofold. First, the coherence length in  $\text{La}_{2-x}\text{Sr}_x\text{CuO}_4$  along the *ab*-axis is 3.2 nm [82]. Hence, the expected proximity length is expected to last 100s of nm. Second, we want to induce this effect using novel ionic liquid (IL) gating techniques. The advantage of using ILs lies in the formation of an electric double layer on the channel surface. The anion/cation separation when applying a gate voltage over the IL is  $\sim 1$  nm, leading to a huge electric field, enough to induce charge carrier densities of  $8 \times 10^{14} \text{ cm}^{-2}$  [109], comparable to the 2D charge carrier densities in cuprates. Hence, this techniques has been used to induce superconductivity in cuprates [10, 66]. This method would then allow us to induce this GPE without having to make a discontinuity in the film. In this chapter we present techniques and preliminary results of a long range effect on a continuous  $\text{La}_{2-x}\text{Sr}_x\text{CuO}_4$  film along the *ab*-axis using IL gating.

## 8.2 Experimental details

We use pulsed laser deposition (PLD) in combination with reflection high energy electron diffraction (RHEED) for the growth of the  $S'$  layer  $\text{La}_{2-x}\text{Sr}_x\text{CuO}_4$  ( $x = 0.05/0.09$ ) on  $(\text{LaAlO}_3)_{0.3}(\text{Sr}_2\text{AlTaO}_6)_{0.7}$  or  $\text{LaSrAlO}_4$ . The deposition proceeds in an oxygen pressure of 0.13 mbar, while the laser fluency used is  $1.5 \text{ J/cm}^2$  (Fig. 8.1a,1). To stimulate the growth to become layer-by-layer, we pause the deposition at each unit cell (UC) for 30 to 60 seconds for the layers to recrystallize before the next deposition of the next UC [143]. By doing so, RHEED oscillations can be observed up to the eventual film thickness of 30 UCs. As the sample is oxygen deficient at deposition, we increase the oxygen pressure after deposition to 0.6 mbar and cool the sample down at a rate of 10 C per min, while waiting at 600 C (15 min) and at 450 C (30 min) (Fig. 8.1a,2). Next, the cuprate film is in-situ covered by a 70 nm layer of Au, again by means of PLD (Fig. 8.1a,3). For this process, we use a deposition pressure of 0.2 mbar of Ar and a laser fluency of  $4.0 \text{ J/cm}^2$ . Photolithography (Fig. 8.1a,4+5) in combination with a  $\text{KI/I}_2/\text{H}_2\text{O}$  (mass ratio 4:1:40) solution is used for the exposure of the channel ( $50 \times 300 \mu\text{m}^2$ ) by wet etching the exposed Au layer (Fig. 8.1a,6). The subsequent steps involve e-beam lithography, as shown in the inset, used to design the  $\text{AlO}_x$  line that will form the barrier. The design of the  $\text{AlO}_x$  layer starts with an electron beam step involving an electron dose exposure of  $300 \mu\text{C/cm}^2$  in the PMMA layer of approximately 240 nm thick (Fig. 8.1a,6,ii). The exposure involves two rectangular shapes ( $2 \times 48 \mu\text{m}^2$ ) connected by a line that will form the barrier ( $0.025\text{-}0.3 \times 4 \mu\text{m}^2$ ), as shown in the schematic topview of the channel area (Fig. 8.1a,6,iii). After development, the written structures are checked by Atomic Force Microscopy (AFM), followed by another process involving the deposition of  $\text{AlO}_x$  (Fig. 8.1a,6,iv) and a lift-off step (Fig. 8.1a,6,v). After the lift-off (Fig. 8.1a,7), the thickness and width of the narrowest part of the  $\text{AlO}_x$  layer are again checked by AFM and subsequent photolithographic steps (Fig. 8.1a,8+9) are used to define areas that are to be dry etched (Ar, 500 V) (Fig. 8.1a,10). The lift-off of the resist is followed by a final check of the barrier by AFM, a typical result of which is shown in (Fig. 8.1b). As a final step, the sample is wirebonded and an IL droplet is put on the channel and gate electrodes. The IL is treated in vacuum conditions in the experimental setup and is pumped

until a pressure of  $1 \times 10^{-4}$  to  $10^{-6}$  mbar is reached before doing any measurements. This is to ensure that electrochemical processes due to water or oxygen present in the IL are minimized. For the same reason, the temperature at which gating (charging temperature) is performed is held between 210 – 225 K, as low as possible, but above the melting point of DEME-TFSI (*N,N*-diethyl-*N*-(2-methoxyethyl)-*N*-methylammonium bis(trifluoromethylsulphonyl)-imide) of 183 K. We use two Keithley SourceMeters (2450) to apply a fixed current of 1  $\mu$ A between the source (S) and drain (D) electrodes, while simultaneously measuring the voltage drop between these two electrodes, either by means of a two-probe or a four-probe configuration. Unless stated otherwise, the measurements performed in this work were based on the four-probe configuration. The distance between the voltage probes is such that the resistance of the channel is equal to the sheet resistance. The other SourceMeter is used to apply a gate voltage ( $V_g$ ) between the gate and drain electrodes (Fig. 8.1a,11).

### 8.3 $AlO_x$ barrier characterization

We deposit a certain amount for the  $AlO_x$  layer, which nominally coincides with an approximate thickness of 95 nm. For various barrier widths, the observed width and thickness of the  $AlO_x$  barrier is plotted with respect to the designed width of the barrier in Fig. 8.2. We observe that both the observed width and thickness of the barrier do not agree with and vary approximately linearly with the designed width. The reduced  $AlO_x$  deposition rate is mainly influenced by the aspect ratio between the thickness of the PMMA layer and the width of the structure developed into the PMMA layer, which is  $\sim 0.1$  for the 25 nm wide barrier. The observed thickness of the  $AlO_x$  barrier at the barrier with a width of 25 nm is 6.0 nm. In contrast, the aspect ratio is close to unity for the widest barrier for which the thickness is 65 nm, close to the maximum possible thickness. Furthermore, we observe a typical widening of the structure vs. the designed barrier width. Remarkably, the widening is not constant but increases as a function of designed width. This is probably due to an excessive electron dose which could lead to some widening effects during the writing or the development processes.

It is crucial for any IL-induced long-range Josephson junction effect to verify whether this is caused by a genuine giant proximity

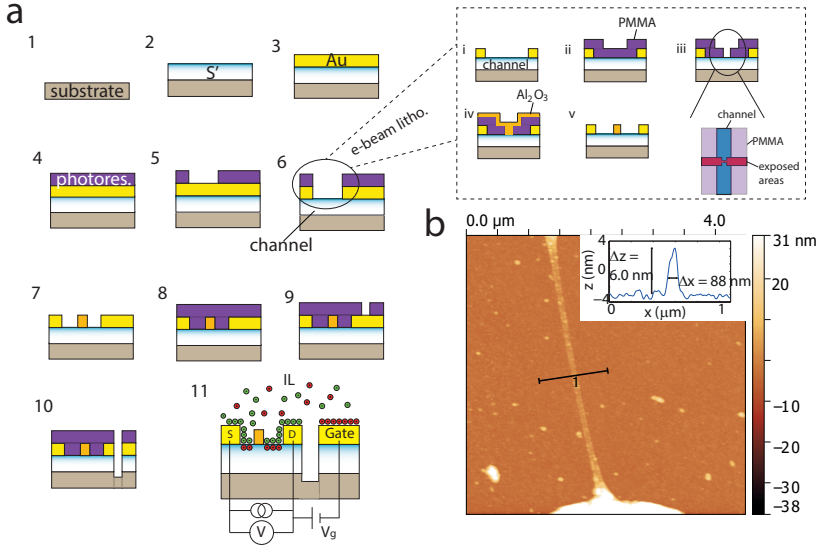


**Figure 8.1:** (a) A schematic overview of the sample fabrication and device setup. 1,2,3) PLD is used to grow  $\text{La}_{2-x}\text{Sr}_x\text{CuO}_4$  and Au. 4,5,6) Photolithographic and wet etching techniques are used to open up the channel area. i,ii,iii,iv,v) Next, e-beam lithography is used to define the barrier. 7,8,9,10) The next photolithographic steps are used to define areas that are to be dry etched. 11) After this process, a lift-off step is followed by wirebonding. The sample is then covered by an IL droplet. (b) An AFM image of a 6.0 nm thick barrier of  $\text{AlO}_x$  for a design width of 25 nm.

effect. The IL gating could, in principle, also affect the barrier area in an unwanted way, for example when ion/oxygen diffusion from or to the barrier area starts to play a role. Firstly, the alumina layer should be sufficiently thick to increase the EDL separation under the barrier as the induced charge carrier density should scale inversely with the barrier thickness. The layers used in this work have a sufficiently large thickness, as the literature suggest a thickness of 2 [63] to 5 nm [72] is enough to minimize the electrostatic charge doping under the barrier area.

The stoichiometry of the  $\text{AlO}_x$  could play a role in oxygen diffusion processes which could affect the  $T_{c'}$  of the  $\text{La}_{2-x}\text{Sr}_x\text{CuO}_4$  layer under the barrier in an unwanted way. The stoichiometry of the alumina is determined by the deposition parameters of oxygen pressure and target substrate distance [166]. Hence, we make sure that  $\text{AlO}_x$  is de-

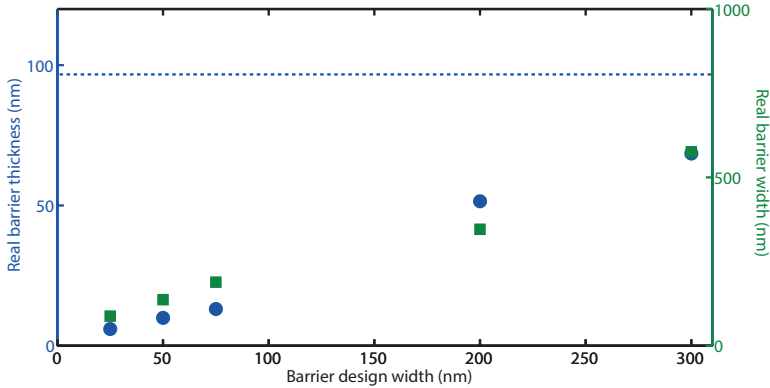


**Figure 8.2:** The real barrier thickness and width plotted vs. barrier design width using 1500 pulses, which nominally coincides with 95 nm (dotted blue line).

posited in a high oxygen pressure of 0.2 mbar along with a maximized substrate-target distance of 60 mm for optimal stoichiometric deposition to prevent oxygen diffusion from the film towards the  $\text{AlO}_x$ , as is the case with  $\text{SiO}_2$  or  $\text{SiN}_3$ . We have observed that samples covered by the latter materials become deep insulators within a time span of days, presumably having to do with the capping layer inducing some oxygen gettering process from the cuprate lattice, rendering it an insulator. Alumina does not have this issue, as  $\text{AlO}_x$  films as thin as 2 nm have been recorded to be near-impermeable for oxygen diffusion [63].

Next, we show experimental data to suggest that IL gating does not influence the layer beneath. For this, a 35 UC  $\text{La}_{1.95}\text{Sr}_{0.05}\text{CuO}_4$  channel is structured in a Hall bar configuration. Using electron beam lithography methods, one part of the channel is covered by a 100 nm layer of  $\text{AlO}_x$  (see Fig. 8.3a). Without any IL gating applied, the samples shows no superconductivity (see Fig. 8.3b) when measured over the area having no  $\text{AlO}_x$  top layer. Applying a gate voltage of -5.0 V approximately 30 minutes at 210 K, the resistance of the film is observed to be 30 % lower near the gating temperature and a superconducting transition is induced at lower temperatures, having a  $T_c$  ( $R = 0$ ) of 18 K. In terms of  $IV$  characteristics, there is a clear difference when measuring the voltage drop at 1.6 K with and

without the  $\text{AlO}_x$  barrier (see inset of Fig. 8.3b) below the  $T_c$  of the gated film. In the latter case, a critical current of approximately  $450 \mu\text{A}$  is observed, while a linear response is measured in the former case. In other words, except for the area of film under the  $\text{AlO}_x$  barrier the whole film has turned superconducting, suggesting that the gating does not affect this area, at least not enough to induce superconductivity along with the rest of the film.

To investigate this further, we deposit a 100 nm thick layer of  $\text{AlO}_x$  on one side of a  $\text{La}_{1.91}\text{Sr}_{0.09}\text{CuO}_4$  channel connected to a Hall bar electrode configuration (see Fig. 8.3c). We observe that minor changes are present in the  $R(T)$  characteristics (Fig. 8.3d). The small differences could well be caused by inhomogeneities or size differences in the film. Furthermore, the  $T_c$  measured as the minimum in  $dR/dT$  is equal, i.e. 6.6 K (see Fig. 8.3d), which shows that the  $\text{AlO}_x$  layer does not influence the superconducting properties of the film.

## 8.4 Experimental results and discussion

With the seemingly neutral properties of  $\text{AlO}_x$  towards IL gating and the oxygen stoichiometry of the  $\text{La}_{2-x}\text{Sr}_x\text{CuO}_4$  film, the gating process is expected to affect only the sectors of the film that are exposed to the IL. Typically, an eventual gate voltage between -5 and -5.5 V is applied in a stepwise fashion, while measuring the gate current and resistance of the film. In the specific example shown in Fig. 8.4, most of the effect is observed for gate voltages below  $-3 \text{ V}$ , accompanied by a process which typically takes in the order of an hour to complete. This is slow compared to the  $RC$  time ( $\sim 0.1 \text{ s}$ ) of the IL/ $\text{La}_{2-x}\text{Sr}_x\text{CuO}_4$  system at these temperatures and has been observed in other IL experiments done on the cuprate  $\text{YBa}_2\text{Cu}_3\text{O}_{7-\delta}$  [62, 63], and was linked to the oxygenation of  $\text{La}_{2-x}\text{Sr}_x\text{CuO}_4$  [63]. This interpretation is further supported by diffusion-limited charge transfer behavior of the gate current, as also described in Chapter 6.

This specific sample has already a superconducting transition  $T_c(R = 0)$  of 4.5 K at  $V_g = 0$  (Fig. 8.5a). It has a 282 nm wide and  $\sim 60 \text{ nm}$  thick  $\text{AlO}_x$  barrier in the same Hall bar-like configuration shown in Fig. 8.3a. By means of IL gating at  $-5.5 \text{ V}$  the oxygenation leads to an increase of the  $T_c$ . Upon cooldown of the sample we observe two distinct critical temperatures, unlike before. The lower (higher)  $T_c$  is attributed to the  $S'$  ( $S$ ) layer (un)covered by the  $\text{AlO}_x$  layer.

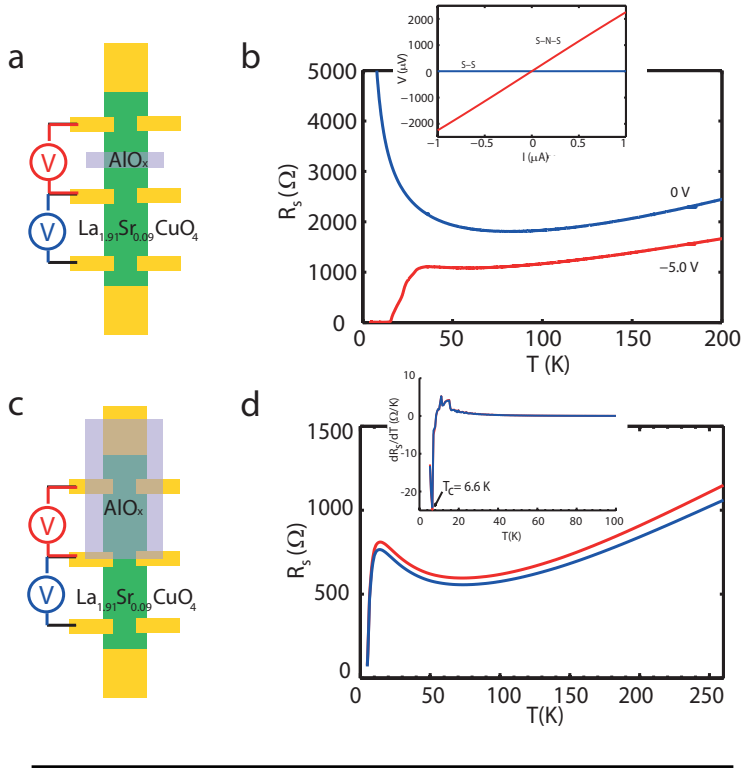


**Figure 8.3:** (a) Sheet resistance curves of a 35 UC  $\text{La}_{1.95}\text{Sr}_{0.05}\text{CuO}_4$  film grown on  $(\text{LaAlO}_3)_{0.3}(\text{Sr}_2\text{AlTaO}_6)_{0.7}$  before (blue) and after (red) gating at  $-5.0$  V. (b) We observe semiconducting behavior at low temperatures initially, while after gating a superconducting transition is induced with a  $T_c$  ( $R = 0$ ) of 18 K. The inset shows  $I$  vs.  $V$  when measured across the superconducting leads of the channel without  $\text{AlO}_x$  barrier layer (blue) shows no voltage induced by the current, which confirms that the film is superconducting. The response is linear when the voltage drop is measured across the  $\text{AlO}_x$  barrier. (c) A four-probe measurement configuration for the purpose of quantifying the influence of a  $\text{AlO}_x$  on the superconducting properties of  $\text{La}_{1.91}\text{Sr}_{0.09}\text{CuO}_4$  grown on  $(\text{LaAlO}_3)_{0.3}(\text{Sr}_2\text{AlTaO}_6)_{0.7}$  in which one side of the channel is covered by the alumina. (d)  $R(T)$  characteristics of both the covered (red) and uncovered cuprate layer. The inset shows the  $dR/dT$  characteristics.

Remarkably, the initial  $T_c$  ( $R = 0$ ) of 4.5 K before the application of the gate voltage increases to 9.5 K. Furthermore, we see a substantial increase in critical current by an order of magnitude ( $1.2 \times 10^2 \mu\text{A}$  to  $1.1 \times 10^3 \mu\text{A}$ ) at 2.0 K (Fig. 8.5b). The numerically calculated differential conductance  $dI/dV$  indicates the presence of peaks at  $\pm 1.6$  mV,

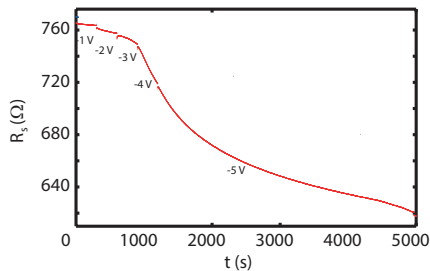


**Figure 8.4:** A typical time development of the sheet resistance of a 30 UC  $\text{La}_{2-x}\text{Sr}_x\text{CuO}_4$  film ( $x = 0.09$ ) grown on  $(\text{LaAlO}_3)_{0.3}(\text{Sr}_2\text{AlTaO}_6)_{0.7}$  upon decreasing the gate voltage in step-wise fashion at a polarization temperature of 225 K. We observe that most of the gating effect happens below  $-3$  V. The gating process takes  $\sim 1$  hour to complete, which is relatively slow when compared to the  $RC$  time of the  $\text{IL}/\text{La}_{2-x}\text{Sr}_x\text{CuO}_4$  system ( $\sim 0.1$  s).

not observed before gating (Fig. 8.5c), although both show a large superconducting peak at zero bias. Here, the sharp zero bias peak represents the transmission of paired charge carriers between the  $S$  leads, while the two broad peaks are interpreted as transmission through Andreev bound states at voltages corresponding to  $\Delta/e$ , typical for  $SNS$  junctions [247, 253, 254], with  $\Delta$  the superconducting gap of the electrodes. As the ratio  $2\Delta/k_B T_c$  is close to the BCS value of 3.52 for low  $T_c$  cuprates such as  $\text{La}_{2-x}\text{Sr}_x\text{CuO}_4$  [247], inserting  $\Delta = 1.6$  meV gives a value of the  $T_c$  of 9.8 K, comparable to the observed values of  $T_c'$ .

In summary, the critical current seems to be preserved over a distance of the barrier width of close to 300 nm, which is  $\sim 100\xi_{ab}$ , while the spectroscopic signal points to the presence of an  $SNS$  junction. Together with the increased  $T_c'$  of the  $\text{La}_{2-x}\text{Sr}_x\text{CuO}_4$  layer under the barrier, these observations all seem to point to a genuine long-range proximity effect. However, there still are some scenarios which can lead to the same observations, and hence need to be discussed in detail.

If the barrier material is even slightly porous for ions, we cannot tell whether the increased  $T_c'$  of the barrier material is caused by a genuine long-range proximity effect. In this case, the role of the quality of  $\text{AlO}_x$  is indeed crucial to the presented picture in this work, for if the  $\text{AlO}_x$  is slightly porous to ions, some of the gating effect is

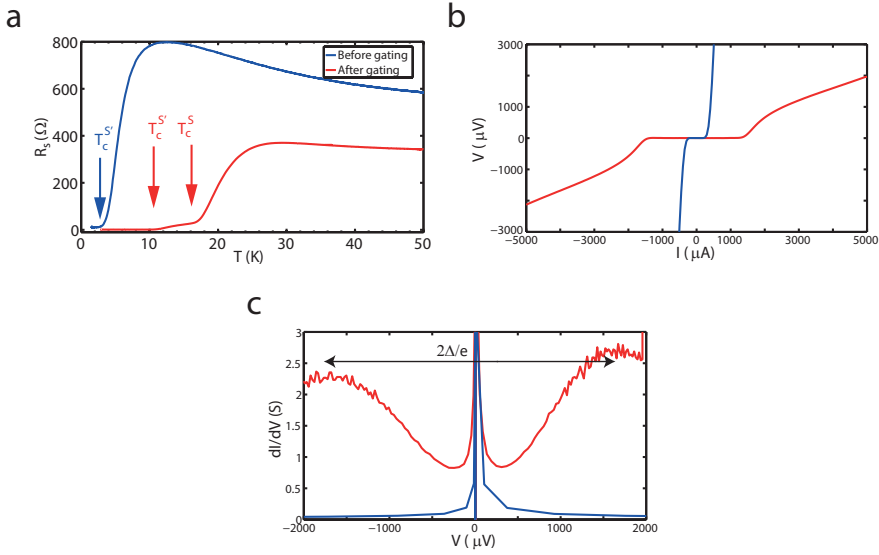


**Figure 8.5:** (a) The  $R(T)$  curve measured over the 282 nm wide  $\text{AlO}_x$  barrier before gating is shown in blue, having a single  $T_c$ . After gating at  $-5.5$  V (red curve), two transition temperatures are observed. The lower  $T_c'$  is assumed to be that of the  $S'$  barrier, while the higher  $T_c$  is coupled to the  $S$  leads. (b)  $IV$  Characteristics of the junction before and after gating. Before gating, the critical current is approximately  $1.2 \times 10^2 \mu\text{A}$ . After gating, this is increased by an order of magnitude to  $1.1 \times 10^3 \mu\text{A}$ . (c) The numerically calculated  $dI/dV$  shows a change in behavior as well. While no structure apart from the main peak at  $V = 0$  is observed before gating, after gating two additional peaks appear at  $\pm 1.6$  mV.

expected to happen directly at the layer of  $\text{La}_{2-x}\text{Sr}_x\text{CuO}_4$  under the barrier due to ion diffusion into the layer, which can lead to some increase in  $T_c'$ . Although the gating effect might be not as much as at the  $S$  leads, the  $I(V)$  characteristics of the junction would still resemble that of the  $SNS$  or  $SIS$  junctions reported before [247].

The likelihood of this scenario depends on the deposition parameters: the oxygen pressure  $p$  and target-substrate distance  $d$ . These influence the kinetic energy of the ablated material and hence crystallinity and structure of the grown  $\text{AlO}_x$ . As stated in Ref. 166, open and porous and stoichiometric  $\text{AlO}_x$  is expected for  $p^{0.5}d \geq 0.4 \text{ Pa}^{0.5}\text{m}$ , while a dense morphology but non-stoichiometric variant is grown for  $p^{0.5}d \leq 0.08 \text{ Pa}^{0.5}\text{m}$ . Although the used settings in this work have been based on optimal oxygen stoichiometry, the grown

material is in between both of these regimes morphologically, meaning, while most samples are non-porous, there are some samples that are indeed permeable to ions. To illustrate this, one sample is covered by a 47 nm thick layer of  $\text{AlO}_x$  on one side of a Hall-bar like channel of  $\text{La}_{1.91}\text{Sr}_{0.09}\text{CuO}_4$  (Fig. 8.6a). A subsequent exposure of both areas to IL gating shows that the  $\text{AlO}_x$  covered area responds to a wide range of the gate voltage in the same way as the exposed area. We observe that, both the barrier and film area before and after gating at -5.5 V (Fig. 8.6b) can show similar  $T_c$ s, as shown in the inset.

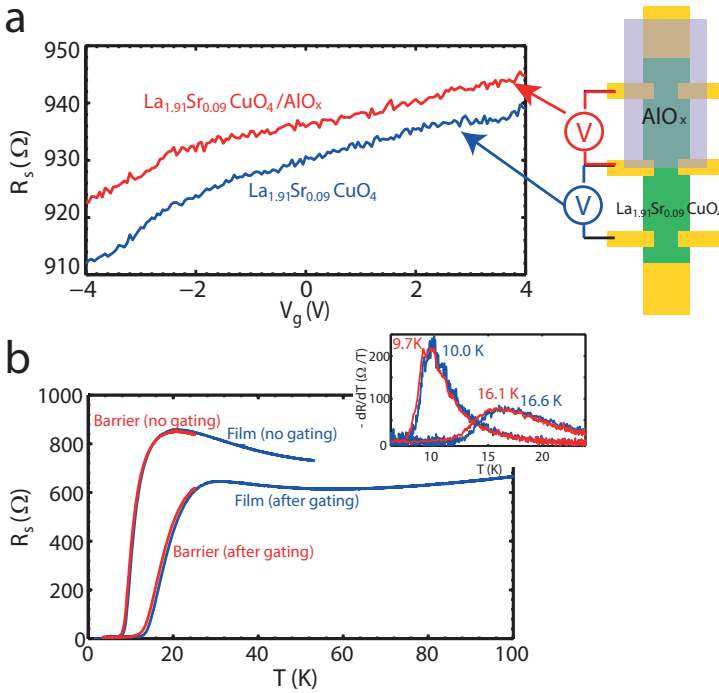


**Figure 8.6:** (a) Comparative  $R(t, V_g)$  behavior of an exposed and alumina covered  $\text{La}_{1.91}\text{Sr}_{0.09}\text{CuO}_4$  film in a Hall-bar configuration. (b)  $R(T)$  characteristics of the barrier and film area before and after gating at -5.5 V. The inset shows the  $dR/dT$  as a measure of the  $T_c$  of the film and barrier areas.

It should be noted that the work presented here is preliminary, as these devices tend to breakdown at elevated voltage drops of  $\sim 5$  mV between the voltage probes ( $\sim 9$  mA). After breakdown, the critical

currents were reduced significantly, dropped to levels similar as before gating. We suspect that this might be caused by electromigration taking place either in the  $\text{AlO}_x$  barrier, or in the  $\text{La}_{2-x}\text{Sr}_x\text{CuO}_4$  layer. The four-probe distance of  $50 \mu\text{m}$  corresponds to an in-plane field of  $1 \times 10^4 \text{ V/cm}$ , which is substantially lower than the required breakdown field of  $\text{AlO}_x$  of  $7 \times 10^6 \text{ V/cm}$  [72]. The  $\text{AlO}_x$  grown in Ref. 72 is of nominal stoichiometry ( $x = 1.5$ ), while the  $\text{AlO}_x$  grown in this work is most probably off-stoichiometry [166], which is known to have a limited breakdown voltage [81], but would still not be enough to explain the three order of magnitude of difference.

We hence suspect that a possible electromigration is more likely to happen in the cuprate layer. If we take into account that at most the top 10 UCs of the layer is conducting due to strain effects, the levels for a breakdown current of 9 mA, and  $50 \mu\text{m}$  wide channel gives a current density of  $1 \times 10^6 \text{ A/cm}^2$ . Such levels of the current densities are reported to be sufficient to induce electromigration in cuprate compounds, e.g.  $\text{YBa}_2\text{Cu}_3\text{O}_{7-\delta}$  [255].

## 8.5 Conclusions

In conclusion, although these results are promising and we have a strong indication of a long-range proximity effect in the *ab*-axis of two orders of magnitude larger than  $\xi_{ab}$ , it is only preliminary, as we cannot exclude the  $\text{AlO}_x$  to be permeable to ions. Furthermore, the sensitivity of the system to breakdown limits the scope of this work to resistance and spectroscopic measurements, as we are lacking measurements of the *IV* characteristics of the junction as function of magnetic field between the initial and new  $T_c$  of the film, 4.5 K and 9.5 K, respectively. Additional data would include the dependence of the critical current as a function of the width of the  $\text{AlO}_x$  barrier. Currently, research on both of these issues is ongoing.

# Chapter 9

## The story continues...

*As described in Chapters 7 and 8, two main methods have been used in an attempt of making an in-plane Josephson junction for the purpose of investigating the giant proximity effect (GPE). In this final chapter we introduce further experiments and combine the information from the previous chapters in order to evaluate the evidence for the in-plane giant proximity effect. We discuss the relevance of these results for various models that have been proposed, and make suggestions for further experiments.*

### 9.1 Ionic liquid induced junction experiments revisited

The possible porosity of the barrier material of  $\text{AlO}_x$  prompted us to delve into methods of overcoming this issue and to redo some of the experiments described in Chapter 8. The method used involves crosslinked poly(methyl methacrylate) (PMMA) as barrier material, which is insoluble in ethanol, acetone and the ionic liquid (IL). The present study presented here only elaborates on positive resist which becomes crosslinked at doses of  $\geq 13000 \mu\text{C}/\text{cm}^2$ , an Atomic Force Microscopy (AFM) image of which can be seen in Fig. 9.1a. The backscatter effect is substantial because of long retention times of the electron beam at a certain spot during writing, resulting in wide ( $\geq 80$  nm) and thick barriers ( $\geq 30$  nm) (see Fig. 9.1b). In this specific case, the length is  $\sim 5 \mu\text{m}$ , while the width is 327 nm, which is comparable to the length and width of the  $\text{AlO}_x$  barrier described in Chapter 8.

The  $\text{La}_{2-x}\text{Sr}_x\text{CuO}_4$  film has a doping of  $x = 0.09$ , 6 unit cells (UC) thick and is grown on top of a metallic buffer layer of 1 UC and doping of  $x = 0.30$ . Before IL gating, both the film without and with

the barrier have similar electrical transport properties and critical temperature ( $T_c$ ) of approximately 35.3 K (midpoint) (see Fig. 9.1c). After IL gating at  $V_g = -5.5$  V for appr. 1 hour, an increase in  $T_c$  of the film without barrier is observed, with the new value being 37.8 K. This is similar to the new  $T_c$  of the film with barrier, except that another transition temperature is present as well (see Fig. 9.1c). When the resistance related to the second  $T_c$  is inflated by a factor of  $95 \pm 8$ , the exact, initial  $R(T)$  curve is recovered, indicating that there is no  $T_c$  change of the barrier material (see Fig. 9.1d). Furthermore, this ratio would coincide with an effective barrier width of  $336 \pm 28$  nm, within the values suggested by AFM data.

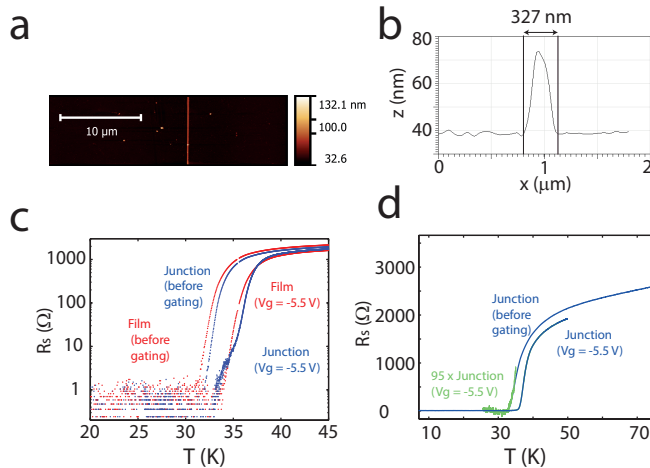


**Figure 9.1:** (a) An AFM image of the film covered with a line of crosslinked PMMA, before the application of IL. (b) The cross section of the barrier, having a thickness of appr. 30 nm and width of 327 nm. (c)  $R_s(T)$  of the film with ('Junction', blue) and without ('Film', red) barrier before and after IL gating at -5.5 V for appr. 1 hour. Only when the resistance is measured across the film do we observe an extra transitional temperature. In (d), the resistance related to this transitional temperature is inflated  $95 \times$  (green) and compared to the resistance of the film with barrier before and after IL gating (blue).

Overall, the data shows that it is possible to successfully make IL gating experiments by means of barriers with crosslinked PMMA without encountering the problems of  $\text{AlO}_x$ . Still, the unchanged  $T_c$  of the barrier material is not supportive of a proximity effect between the leads, at least for the  $T_c$  and the barrier widths described in the present study. This is unexpected, as the barrier width is within the ab-axis GPE range reported previously.

The first explanation is, as described in Chapter 1, is the one based on the phase-disordered superconductors model proposed by Marchand *et al.* [35], which proposes that the proximity of the bulk superconductor prevents the unbinding of the vortex-antivortex pairs at the nominal barrier  $T_{c'}$ . This leads to a logarithmic dependence of the barrier  $T_c$  on the barrier width  $d$  and hence a significant enhancement of the supercurrent at temperatures above the initial nominal barrier  $T_{c'}$ ,

$$T^{eff} \cong T_c \left[ 1 - \left( 1 - \frac{T_{c'}}{T_c} \right) \frac{\ln(d/\xi)}{\ln(L/\xi)} \right]. \quad (9.1)$$

Here,  $d$ ,  $\xi$  and  $L$  stand for the barrier width, the coherence length and length of the superconducting leads, respectively.  $T_c$  and  $T_{c'}$  represent the critical temperature of the  $S$  and  $S'$  layers, respectively. Using the experimentally obtained parameters for the fitting ( $d = 300$  nm;  $L = 5000$  nm;  $T_c = 37.8$  K;  $T_{c'} = 35.3$  K and  $\xi = 3.2$  nm) results in the expected barrier critical temperature as a function of the critical temperature of the leads (see Fig. 9.2).

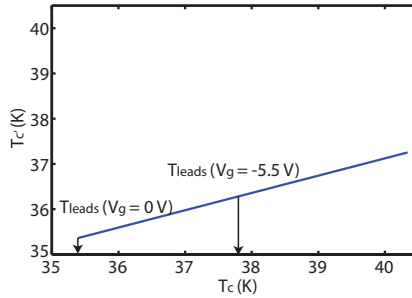


**Figure 9.2:**  $T_{c'}$  as a function of the lead  $T_c$  of the junction shown in Fig. 9.1 according to relationship found in Marchand *et al.* [35].

The expected value for  $T_{eff}$  is 36.3 K, however the empirical value found after gating is still 35.3 K. Although the experiment requires extension to other  $T_c$  and  $T_c'$  values and other barrier widths, the tentative conclusion is that the proximity effect does not extend as far as predicted by the model of Marchand *et al.*

## 9.2 Etched bilayers

The first method involved an ion etched quasi-*ab* junctions in bilayers of  $\text{La}_{2-x}\text{Sr}_x\text{CuO}_4/\text{YBa}_2\text{Cu}_3\text{O}_{7-\delta}$ . This method proved to be successful in achieving a genuine  $T_c$  change of the barrier material over distances of  $\sim 50$  nm, coupled with a robust  $I_c$  (using a  $1 \mu\text{V}$  criterion) above its former critical temperature,  $T_1 = 4.5$  K (see Fig. 9.3a).

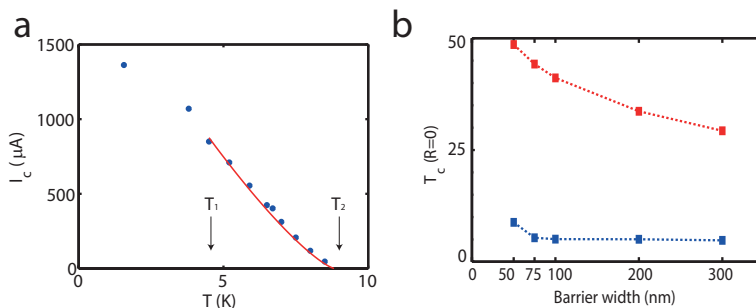


**Figure 9.3:** (a)  $I_c(T)$  of the etched bilayer for a barrier width of 50 nm. At low  $T$ , the curve is characterized by a slow decrease, after which a nearly linear regime sets in. Only at temperatures close to  $T_c$  does the  $I_c$  curve upward, which allows fitting the percolation based relationship  $I_c \propto \left(\frac{T}{T_c} - 1\right)^p$ . The fitted curve starts from the default  $T_c$  of  $\text{La}_{1.91}\text{Sr}_{0.09}\text{CuO}_4$ ,  $T_1 = 4.5$  K until  $T_2 = 8.6$  K. (b)  $T_c(R=0)$  values plotted as a function of barrier widths used in the etched bilayers (blue), compared with Marchand's relationship for the expected effective barrier  $T_c$  (red).

The data presented is also compared with Marchand's picture of (un)binding vortices in the pseudogap phase. Using  $T_c' = 4.5$  K;  $T_c = 78.2$  K;  $L = 3 \mu\text{m}$  and  $\xi = 3.2$  nm, the values for the barrier  $T_{eff}(d)$  are calculated and compared with the experimental data (see Fig. 9.3b). As a note, caution is required as the barrier is not entirely along the *ab*-axis, but is rather quasi-*ab* in nature. Still, the expression is only logarithmically dependent on our parameters for  $L$ ,  $d$  and  $\xi$ , and the

resulting dependence does not fit the experimental  $T_{eff}(d)$ . Hence, we have to conclude that the data presented here for the etched bilayers, in accordance with the data for the IL-gated junctions, are not in line with the vortex (un)binding theory of Marchand *et al.* [35].

Explanations invoking the divergence of coherence length expected based on the de Gennes formalism, as has been applied in the Pb/Si(111) system [21], are not satisfactory as well. Firstly, the formalism predicts that the coherence length should diverge when  $T_c$  is approached from above, either as  $\sim 1/\sqrt{T - T_c}$  (dirty limit), or as  $\sim 1/(T - T_c)$  (clean limit). The mean free path in the  $S'$  material in our case along the  $ab$ -axis is estimated to be 1-2 nm, which is close to the coherence length of about 3 nm along the same direction. In either limiting cases applicable, the highest and lowest  $T_c$  of the junction, 8.6 K and 4.5 K, respectively, used to obtain  $\xi = 1.4\xi_0$  or  $2.0\xi_0$ , which are only small corrections compared to the width of the junction.

Instead, we see a power law behavior which is in line with the theory developed by Kresin *et al.* [36] of percolation-driven connection of superconducting islands, in line with the picture of preformed pairs in the pseudogap phase (see Chapter 1). In Fig. 9.3a this is illustrated by fitting the data between  $T_1 \leq T \leq T_2$  with  $I_c \propto \left(\frac{T}{T_c} - 1\right)^p$ , which results in power law exponent of  $p = 1.29 \pm 0.15$ , in agreement with the value  $4/3$  for the critical index known in the percolation theory, which itself is in agreement with experimental work on the GPE in  $\text{La}_{2-x}\text{Sr}_x\text{CuO}_4/\text{La}_2\text{CuO}_4/\text{La}_{2-x}\text{Sr}_x\text{CuO}_4$   $c$ -axis junctions by Bozovic *et al.* [36]. However, microshorts cannot be excluded in this work, especially because of the inhomogeneities involved in etching.

### 9.3 Conclusions and experimental outlook

To conclude, the data presented in this thesis concerning the etched bilayers and the IL-induced junctions does not support the theory based on vortex-antivortex (un)binding in the pseudogap phase as stated in Ref.35 (see Table 9.1). The de Gennes formalism has found no backing in our experiments, while we have found that the long-range proximity effect observed in the etched bilayers do support percolative transport of the supercurrent via superconducting puddles. This is quite interesting, as this can be connected to the pseudogap picture as a whole, and specifically that of phase fluctuations in accordance with Kresin's theory [36].

Explanation	Ionic liquid induced junctions	Etched bilayers
Phase-disordered superconductor [35]	No	No
de Gennes formalism [21]	-	No
Superconducting puddles [36, 37]	-	Likely

**Table 9.1:** List of explanations coupled to the observations of the IL-induced junction and etched bilayer experiments.

Experimentally, there is some space for a more thorough look at the possible role of phase fluctuations in the long-range effect, where the most acute need is the investigation of the  $I(V)$  characteristic of the junction firstly for various barrier widths, and secondly for a wider range of  $T_c$  of the leads. For the latter dependence, IL gating is an ideal method because of the flexibility in applying various gate voltages. Overall, the proposition would involve barriers widths (see Fig. 9.4), ideally covering at least length scales varying two orders of magnitude or more, starting from  $\sim 10$  nm. The current method of crosslinking PMMA, giving a minimum attainable width of  $\sim 80$  nm due to backscatter effects. Therefore, usage of negative e-beam resist such as the AR-N 7520, which crosslinks at a much lower dosage of  $30 \mu\text{C}/\text{cm}^2$  at an acceleration voltage of 30 kV, is advised. The minimized the backscattering effect ensures an attainable width is 6 nm with an aspect ratio of 10.

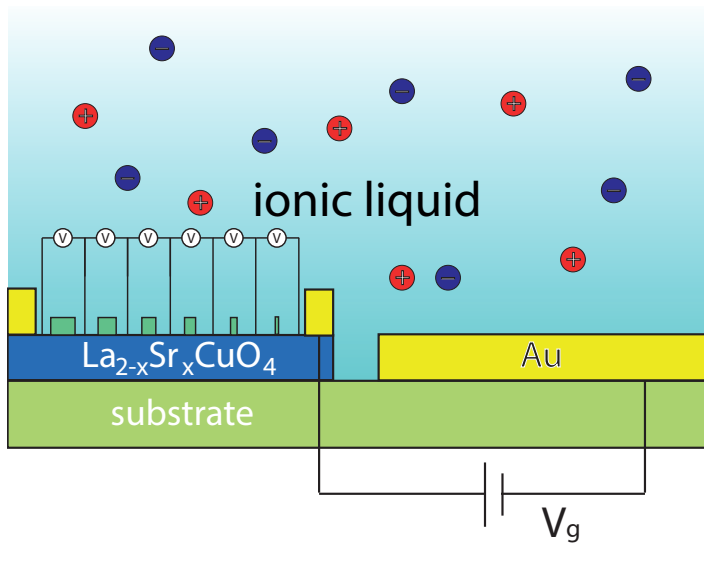
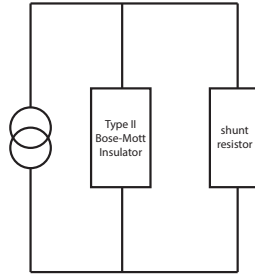


**Figure 9.4:** A proposed experimental setup for a further investigation of the GPE. The main aim of such an experiment is the barrier width dependence and the lead  $T_c$  dependence of the long-range effect for possible reinterpretation of the pseudogap phase. The barrier widths are varied two orders of magnitude using negative e-beam resist, starting from  $\sim 10$  nm, while the IL is used for control of the lead  $T_c$ .

## 9.4 The elusive Type-II Bose-Mott insulator

The long-range proximity effect reported here in the etched bilayers could fulfill the conditions required by Beekman *et al.* [42] for the observation of quantized current filaments. The model starts from a Bose-Mott insulator in its insulating phase (which may be represented by  $\text{La}_{2-x}\text{Sr}_x\text{CuO}_4$  in its pseudogap phase) and is sandwiched between superconducting leads ( $\text{YBa}_2\text{Cu}_3\text{O}_{7-\delta}$ ). The barrier should be in its Bose-Mott insulating state, and current biases smaller than the current quantum  $I_0 \sim 1$  mA (see Section 1.3.2) should not lead to any conduction [42]. This, however, is not observed. Although our observations do not give any evidence, this does not exclude the existence of the Type-II Bose-Mott insulator. A more dedicated experiment could involve current biasing the candidate for the Type-II Bose-Mott insulator using a parallel circuit which would have a shunt resistor (see Fig. 9.5).



---

**Figure 9.5:** A schematic representation of an experiment which involves current biasing the idealized type-II Bose-Mott insulator in parallel with a shunt resistor.

---

The function of this would be that of a vacuum by-pass for the current: in case the Type-II Bose-Mott insulator has not produced its first current quantum, the resistance of the Bose-Mott insulator theoretically is infinite, and the current can still flow through the shunt resistor. Continuously increasing the current until  $I_0$  is reached would suggest that the first Mott vortex should nucleate at the Type-II Bose-Mott insulator and the voltage drop across the Bose-Mott insulator should become zero. In principle, this process is repeatable until the  $2^{nd}$ ,  $3^{rd}$ ,  $n^{th}$  Mott vortex is formed, and in terms of an  $V$  vs.  $I$  characteristic, a sawtooth-like pattern should be observable.

This method of a vacuum by-pass for the current can be used in other systems which show interesting interplays between the electrical current and magnetism. A prominent system for this was found recently in the Mott-insulator  $\text{Ca}_2\text{RuO}_4$  [256], for which strong diamagnetism is reported induced by a dc electrical current. The material is characterized by high resistivity at low temperatures, comparable to the situation when the Type-II Bose-Mott insulator has not yet formed the first Mott vortex. Furthermore, the ruthenate is ill characterized in this highly resistive regime, and by using the vacuum by-pass method, the unexplored regions of this interesting material can be explored, quite possibly making some connections with the present theory of the Type-II Bose-Mott insulator.